Enhancement and Validation of VPM-Derived State-Space Inflow Models for Multi-Rotor Simulation

Matthew Gladfelter, Chengjian He, and Chongseok Chang
Advanced Rotorcraft Technology, Inc.
Sunnyvale, CA 94085, USA

Mark B. Tischler and Mark J.S. Lopez
CCDC Aviation & Missile Center (AvMC)
Moffett Field, CA 94035, USA

Ondrej Juhasz
US Naval Academy
Annapolis, MD 21402, USA

Abstract

State-space inflow models have long been the standard for rotor wake modeling for flight dynamics and control simulation. As rotorcraft design continues to trend toward Future Vertical Lift (FVL) multi-rotor configurations in order to overcome the limitations of traditional design, the use of state space inflow models must similarly evolve to capture the complex aerodynamic interactions inherent to these new rotorcraft configurations. There is a demand for a state-space inflow model that accurately captures the significant aerodynamic interactions that occur between multiple rotors, ducted fans, wings, and complex airframes that preexisting inflow formulation fails to address. This paper discusses the ongoing effort to establish a robust methodology for deriving a state-space inflow model suitable for FVL applications from first-principle based viscous Vortex Particle Method (VPM) using the CIFER® system identification tool. The paper focuses on areas of enhancement that expand the identified inflow model's accuracy and usefulness as a tool for flight dynamics simulation of multi-rotor configurations. First, the effects of wake distortion due to rotor tip-path plane (TPP) rotation are thoroughly investigated for a co-axial configuration across a number of airspeeds and implemented into the inflow model formulation for improved simulation accuracy. Next, the rotor interference on the aerodynamic surfaces and the fuselage is explored, with attention placed on addressing this interference as a unified formulation. For the rotor interference on fuselage (3-D body) estimation, investigation of improvement through multi-point sampling is performed. The paper also examines the control design application through constructing the linear time invariant aircraft model with integrated state-space inflow model and verifying the accuracy of gain and phase margins and crossover frequencies. For each of these areas of investigation, the impacts on precision flight dynamics simulation are assessed through frequency and time domain response analysis and comparison to the simulation with first principle based VPM. The validation results of the predicted response data show excellent agreement with VPM simulation and further justify this method of inflow model identification as an effective tool for multi-rotor and FVL applications.

Nomenclature

C_T	Rotor thrust coefficient
C_L	Rotor hub roll moment coefficient
C_M	Rotor hub pitch moment coefficient
$G.M.$	Gain Margin
$[H]$	Interference gain matrix
J	Frequency domain cost function
J_{AVE}	Averaged fitting cost
K_{rot}^i	$i-$th Rotor wake distortion effect parameter
K_r	Conventional wake distortion effect parameter
$[L]$	Inflow influence coefficient matrix
L_{CFD}	Fuselage lift force determined by CFD analysis
$\tilde{L}$	Effective fuselage lift force
l_j	Fuselage sampling point distance factor
$[M]$	Inflow apparent mass coefficient matrix
N	Number of fuselage interference sampling points
$P.M.$	Phase Margin
p, q	Body roll and pitch rate, respectively
R	Rotor radius (ft)
r	Non-dimensional blade radial position
S_{hub}	Co-axial rotor hub separation distance (ft)
t	Simulation time
TPP	Rotor Tip-Path-Plane
$[V]$	Inflow mass flow parameter

V_{tip}	Rotor tip speed ΩR
$w_i(r, \psi, t)$	i−th Rotor inflow over the rotor plane
$\vec{w}_{intf}$	Rotor induced interference velocity (off-rotor)
$\tilde{\vec{w}}_{intf}$	Effective rotor interference velocity on fuselage
x_b	Longitudinal control
x_a	Lateral control
x_c	Collective controls
x_p	Pedal controls
α_n^{mci}	i−th Rotor inflow states (cosine components)
α_n^{msi}	i−th Rotor inflow states (sine components)
α_1^{0c1}	Upper rotor uniform inflow state
α_2^{1c1}	Upper rotor cosine inflow state (1st harmonic)
α_2^{1s1}	Upper rotor sine inflow state (1st harmonic)
$\tilde{\alpha}_n^{mci}$	i−th Rotor inflow expansion coefficient (cosine)
$\tilde{\alpha}_n^{msi}$	i−th Rotor inflow expansion coefficient (sine)
β_c	TPP longitudinal tilt angle
β_s	TPP lateral tilt angle
λ_f	Freestream inflow normalized by ΩR
λ_i	Uniform induced inflow normalized by ΩR
μ	Rotor advance ratio
Ω	Rotor speed [rad/sec]
$\phi_n^m(r)$	Inflow radial shape function
ψ	Rotor azimuth
τ	Interference time delay from rotor to rotor
τ_h	Interference time delay for off-rotor
τ_i	Inflow state response time delay
τ_k	TPP rotation effect time delay
τ_n^{mc}	Inflow forcing function (cosine components)
τ_n^{ms}	Inflow forcing function (sine components)
τ_1^{0c}	Thrust based inflow forcing function
τ_2^{1c}	Hub pitch moment based inflow forcing function
τ_2^{1s}	Hub roll moment based inflow forcing function
ω_G	Gain crossover frequency
ω_{180}	Phase crossover frequency

Introduction

The widely used finite state (i.e. state-space) inflow model established in Ref. [1] and [2], while suitable for conventional helicopter design, does not include the formulation necessary to simulate the mutual wake interactions of multi-rotor configurations. To address this shortcoming, numerous recent research efforts endeavor to bridge the state-space inflow model with multi-rotor phenomena. References [3], [4], and [5] take the potential flow function based analytical approach as an attempt to accomplish this, while References [6] to [11] explore methods of model parameter identification from high-fidelity rotor wake models. The investigations presented in this paper offer

an extension of the research examined in Ref. [8] that focuses on the latter approach. The high-fidelity wake simulation used is the first-principle base viscous vortex particle method (VPM) (Ref. [12]) while the tool used for inflow model parameter identification is CIFER® system identification (Ref. [13]).

VPM simulation provides accurate rotor induced flow variation information at a much more computationally efficient rate than a full CFD flow solver, and has been widely validated as a precision simulation tool for complex, multi-rotor configurations (Ref. [12]), but it is not formulated in state-space and therefore, cannot be directly utilized for control design and stability assessment. Reference [8] provides detailed description of the process developed to accomplish accurate state-space inflow model identification and validates the fidelity of inflow models identified by the methodology for single and co-axial rotor configurations against measured and simulation data for mostly in hover flight. While the effects of wake distortion due to TPP rotation and rotor induced interference are accounted for in the formulation, their inclusion in the flight dynamics validation was only superficially explored in the previous paper.

The investigations presented in this paper seek to provide an extended exploration of the TPP rotation and rotor induced interference effects, and how the proposed formulation accommodates them. Wake distortion due to TPP rotation covers the additional changes in the dynamic inflow geometry due to the rotations of the rotor hub and TPP as vehicle flight condition changes. Research efforts such as Refs. [14] through [17] discuss the importance of the wake distortion effects as they pertain to single main rotor vehicles and its notable influence on the off-axis response. Rotor induced interference effects in the context of this paper involve the mutual interaction of co-axial rotor wake, the interference velocity experienced by fuselage and aerodynamic surfaces caused by the unsteady wake of each rotor. The importance of capturing such effects is noted in Ref. [18]. The influence of including these effects on the identified state-space inflow model and finally on the overall flight dynamics and control of a co-axial vehicle for both hover and forward flight is thoroughly examined herein. Rotor interference modeling is investigated for multiple rotors and extended to all inflow states under a broad range of flight conditions. The TPP rotation and rotor interference effects are assessed for the integrated full flight simulation in FLIGHTLAB (Ref. [19]) for a co-axial vehicle configuration developed in Ref. [20].

$$w_i(r, \psi, t) \;=\; \sum_{m=0}^{\infty} \sum_{n=m+1,m+3,\cdots}^{\infty} \phi_n^m(r)[\alpha_n^{mci}(t)cos(m\psi) + \alpha_n^{msi}(t)sin(m\psi)] \tag{1}$$

$$States: \quad \begin{bmatrix} M \end{bmatrix}_i \left\{ \begin{array}{c} \dot{\alpha}_m^{mci} \\ \dot{\alpha}_n^{nsi} \end{array} \right\} + \begin{bmatrix} L \end{bmatrix}_i^{-1} [V]_i \left\{ \begin{array}{c} \alpha_n^{mci} \\ \alpha_n^{msi} \end{array} \right\} = \left\{ \begin{array}{c} \tau_n^{mci}(t-\tau_i) \\ \tau_n^{msi}(t-\tau_i) \end{array} \right\} + \begin{bmatrix} \frac{K_{rot,i}}{\tau_k^i S+1} \end{bmatrix} \left\{ \begin{array}{c} q + \dot{\beta}_{1c} \\ p + \dot{\beta}_{1s} \end{array} \right\} \tag{2}$$

$$Outputs: \quad w_{ji}^{intf}(r_j, \psi_j, t) = \begin{bmatrix} H \end{bmatrix}_i^j \left\{ \begin{array}{c} \alpha_n^{mci}(t-\tau_h) \\ \alpha_n^{msi}(t-\tau_h) \end{array} \right\} \tag{3}$$

Unified Inflow Model Formulation

The studies described in this paper continue the use of the multi-rotor inflow formulation used in the previous studies of Ref. [7] and [8]. The finite state inflow model is structured with state and output equations where the state equation governs an individual rotor's inflow dynamics while the output equations formulate the influence of the rotor inflow on other rotors, surfaces, locations, etc. First, the induced inflow distribution equation is presented in the form of Equation 1.

Equation 1 describes the inflow distribution over the i-th rotor of a multi-rotor system. In this equation, α_n^{mci} and α_n^{msi} are the inflow states of the i-th rotor, $\phi_n^m(r)$ is the radial inflow variation shape function, and $w_i(r, \psi, t)$ is the induced inflow distribution described by radial position, azimuthal position, and instance in time.

For the i-th rotor, the inflow dynamics and output formulation is described by Equations 2 and 3, respectively. For these equations, i and j represent the rotor index for the i-th and j-th rotor such that w_{ji}^{intf} is the interference of the i-th rotor on the j-th rotor. The inflow dynamics are dependent on the parameters of the apparent mass matrix $[M]$, inflow influence coefficient matrix $[L]$, and time delay τ_i while the output equation is controlled by the parameters in the interference gain matrix $[H]$ and time delay τ_h. It is these parameters that must be identified accurately in order to properly capture the rotor inflow and influence in simulation. The term $[V]$ is the mass flow parameter and is a function of rotor thrust and flight speed (Ref. [2]). For each rotor, τ_n^{mci} and τ_n^{msi} are the inflow forcing functions with harmonic variation index m, cosine or sine harmonic denotation c or s, and polynomial order of radial shape function n. The terms α_n^{mci} and α_n^{msi} represent the inflow states with similar superscript and subscript definitions. The structure assessed in this paper uses three inflow states allowing for accurate inflow representation while maintaining

easily identifiable 3-by-3 parameter matrices for each rotor. For a configuration of N rotors, only N sets of 3-by-3 parameter matrices must be identified for full inflow simulation.

The state equations also include a term to capture the rotor TPP rotation effect. K_{rot} and τ_k form the transfer function used to capture the TPP maneuvering effect when applied to the sum of the hub pitch rate q and longitudinal cyclic flapping rate $\dot{\beta}_{1c}$ or hub roll rate p and lateral cyclic flapping rate $\dot{\beta}_{1s}$. K_{rot} can be related to the conventional K_r factor (such as described in Ref. [14] and Ref. [15]) with the following:

$$K_{rot,i} = \sqrt{\frac{2}{15}} L^{-1} V K_{r,i} \tag{4}$$

The parameters of K_{rot} and τ_k must also be identified. The identification methodology developed and described in this paper includes a robust procedure for the identification of these parameters in addition to those of the inflow matrices.

Rotor Interference on Aerodynamic Surfaces and Fuselage

A significant amount of the research effort discussed in this paper covers the modeling of rotor interference on the fuselage and aerodynamic surfaces. The formulation for this interference uses the structure of Equation 3 and is presented as

$$\omega_{ji}^{intf} = \begin{bmatrix} H \end{bmatrix}_i^j \left\{ \begin{array}{c} \alpha_n^{mci}(t-\tau_h) \\ \alpha_n^{msi}(t-\tau_h) \end{array} \right\} \tag{5}$$

where w_{ji}^{intf} is the interference of the i-th rotor on the j-th surface or point. Therefore, the fuselage and each surface requires the identification of a corresponding interference matrix for each rotor. For the three state inflow structure used in this research, Equation 5 can be expanded to the following:

$$\left\{ \begin{array}{c} u \\ v \\ w \end{array} \right\} = \begin{bmatrix} h_{11} & h_{12} & h_{13} \\ h_{21} & h_{22} & h_{23} \\ h_{31} & h_{32} & h_{33} \end{bmatrix}_1 \left\{ \begin{array}{c} \alpha_1^{0c1}(t-\tau) \\ \alpha_2^{1c1}(t-\tau) \\ \alpha_2^{1s1}(t-\tau) \end{array} \right\}$$

$$+ \begin{bmatrix} h_{11} & h_{12} & h_{13} \\ h_{21} & h_{22} & h_{23} \\ h_{31} & h_{32} & h_{33} \end{bmatrix}_2 \left\{ \begin{array}{c} \alpha_1^{0c2}(t-\tau) \\ \alpha_2^{1c2}(t-\tau) \\ \alpha_2^{1s2}(t-\tau) \end{array} \right\} \quad (6)$$

This equation structure illustrates the individual parameters that are to be identified to fully capture the interference characteristics for the co-axial rotor configuration. The interference velocity as a vector of directional components allows for ease of implementation into the simulation model.

For the rotor interference on fuselage specifically, an investigation was conducted to determine if an effective interference velocity averaged from a series of sampling points across the fuselage surface could yield a more accurate identified model versus sampling at the c.g. as was done in Ref. [8]. The formulation for this effective interference velocity is

$$\tilde{\vec{w}}_{intf} = \sum_{j=1}^{N} \frac{l_j \vec{w}_{intf,j}}{N} \quad (7)$$

where $\tilde{\vec{w}}_{intf}$ is the effective velocity averaged from N sample points with the weighting l_j applied. l_j is the nondimensionalized offset factor of point j with respect to the moment center to account for the interference influence on the fuselage moments.

Inflow Model Parameter Identification and Verification

The identification methodology developed in Ref. [7] and enhanced in [8] was applied to a generic co-axial vehicle designed based on the study conducted in Ref. [20]. Figure 1 presents the co-axial vehicle configuration. The identification methodology is outlined in Figure 2 with the critical steps as follows:

- A multi-rotor model is created and coupled with VPM inflow. The vehicle fuselage is included so that wake blockage effects are accounted for. The rotor model is run at the flight condition of interest while a 90 second frequency sweep excitation is applied to one rotor through a forcing function. The response of each rotor's inflow states as well as the rotor interference at points of interest are collected during the run. Therefore, mutual interference between rotors is captured for multiple rotor configurations.

- CIFER® is used to determine frequency domain responses from the VPM-generated time histories. From the frequency responses, CIFER® identifies a finite state inflow model through fitting cost optimization. For the inflow model identification application, an automated tool was developed via the Command Line Interface to conduct the process in batch.

- The identified inflow model is verified in both the frequency and time domain to ensure that accurate parameters were obtained. VPM is run as the baseline response to judge accuracy.

- The identified inflow model is integrated into a flight simulation model. The current implementation for a FLIGHTLAB simulation model is table lookup. The full vehicle flight dynamic response is then evaluated.

Using this process, an identified inflow model was developed for the co-axial configuration described. A co-axial rotor model was constructed with VPM coupling, and forcing function excitations with characteristics illustrated in Figure 3 were applied to generate inflow state frequency response data. Figure 4 shows the upper rotor inflow state and lower rotor expansion coefficient response for an upper rotor cosine excitation (second excitation shown in Fig 3) generated from the VPM-coupled coaxial rotor model at 40 knots as an example of the frequency response data of interest. CIFER® was used to construct the identified 3-state inflow model from these time histories. Figure 5 shows the upper rotor cosine inflow state frequency response for this 40 knots flight condition for both the VPM data and the identified inflow model. A fitting cost of J_{AVE} = 72.1 was achieved for this particular response, which is well within the $J_{AVE} \leq 100$ threshold for satisfactory fit as described in Ref. [13]. The automated identification process proved robust for the generic co-axial rotorcraft model with only the flight condition of descent in hover requiring manual tuning of the identified model to achieve satisfactory cost values.

The identified co-axial rotor inflow model was then verified in the time domain by step response analysis. The VPM coupled multi-rotor model is run to establish the truth response, then the identified inflow model response is compared. Figure 6 illustrates the step response of the upper rotor inflow states and Figure 7 the lower rotor interference inflow expansion coefficients from a step excitation of the upper rotor hub pitch moment based inflow forcing function. The identified inflow model accurately reproduces the magnitude changes of the step response indicating an excellent identification.

An important detail of this identification process is that the rotor on rotor mutual interference is determined alongside the individual rotor inflow state parameters. Since both rotors are present when the VPM coupled response data is generated, the same run is used in the identification of $[M]$, $[L]$, and τ_i in Equation 2 as for $[H]$ and τ_h in Equation 3. By determining the mutual rotor interactions in this manner, the identification methodology captures a critical multi-rotor phenomenon in a way that naturally progresses from the inflow state identification process.

Rotor TPP Rotation Effect

While the identification process described in the previous section has been proven as a robust method for establishing an accurate base inflow model, an additional term is required to model the distortion effects that occur as caused by the rotor TPP rotation. An additional identification procedure was developed and conducted to obtain values of K_{rot} and τ_k as formulated in Equation 2. This section details the rotor TPP rotation identification process, verification of the identified parameters, and the resulting impacts on the full vehicle flight dynamics. Emphasis is placed on applications not addressed in Ref. [8] such as integration into a linear flight dynamics model and identification at transitional airspeeds.

Rotor TPP Rotation Identification and Verification

The method used to determine the TPP rotation effect parameters is similar to the inflow model identification process. A VPM-coupled multi-rotor simulation model constructed in FLIGHTLAB is excited with hub frequency sweep rotations of an individual rotor. The same FLIGHTLAB simulation model used in the inflow model identification can be used in TPP rotation effect parameter identification. For the generic co-axial configuration, frequency sweeps of a hub's rotation rate were performed over 90 seconds with an 8 degrees per second amplitude (allowing for the largest excitation without crossing TPPs). As with inflow model identification, the sine and cosine inflow state time histories were recorded from the rotor response to the hub rotation excitations. Whereas the study conducted in Ref. [8] only determined the rotation effect for hover, this paper explores identification for forward flight as well - hover, 15 knots, 40 knots, and 80 knots were assessed for the co-axial rotor model. Figure 8 presents the VPM wake for the hover flight condition at a point in time during the lower rotor

hub rotation where the aft side of the lower rotor is rotated downwards relative to the stationary upper rotor. Asymmetry in the wake is evident as caused by the rotation of the TPP. For forward flight, however, any impact on the wake is largely masked by the freestream velocity as seen in Figure 9.

The time histories of the rotor inflow states and rotation rate are used in CIFER® to generate a frequency response from which the rotation effect parameters are identified. A second order transfer function is fit to the frequency response with a gain corresponding to K_{rot} and two denominator terms corresponding to the inflow time delay τ_i and the rotation effect time delay τ_k. The second order structure was required to achieve an accurate model and is consistent with the findings of Ref. [10] and [14]. τ_i is predetermined from the inflow model identification while τ_k must be identified. Identification of these parameters is performed for each combination of sine or cosine inflow state and p or q hub rotation rate.

Figures 10 through 12 provide an example frequency response and CIFER® fit for each of the flight conditions tested. Figure 10 shows the fit at hover for the lower rotor inflow state response to hub pitching rotation. The second order transfer function fits the response well in frequencies with sufficiently high coherence. As seen in Table 1, the identified rotation time delay of $\tau_k = 2.1$ seconds suggests that rotation effects propagate at an order of magnitude slower than the rotor inflow dynamics. In Figures 11 and 12, similar trends are seen for transitional flight speeds with good fit obtained by the second order model. An identification of TPP rotation effect parameters was attempted at 80 knots, however, it was found that the coherence between inflow states and rotation rate is too low to establish an accurate fit. This suggests that the TPP rotation effect has largely dissipated with the freestream velocity, agreeing with the experimental trend shown in Ref. [14]. As such, K_{rot} is assumed to be zero for airspeeds 80 knots and faster for this particular co-axial configuration.

The identified gains and time delays for the TPP rotation effects are tabulated in Table 1 for hover, Table 2 for 15 knots, and Table 3 for 40 knots.

Table 1: Identified K_{rot} factors and time constants for the generic co-axial rotor in hover

Frequency Response	Rotor Excited	K_{rot}	K_r	τ_i	τ_k
α_2^{1c1}/q	Upper	0.043	0.40	0.188	2.0
α_2^{1c2}/q	Lower	0.060	0.37	0.144	2.1
α_2^{1s1}/p	Upper	0.043	0.40	0.188	2.0
α_2^{1s2}/p	Lower	0.060	0.37	0.144	2.1

Table 2: Identified K_{rot} factors and time constants for the generic co-axial rotor at 15 knots

Frequency Response	Rotor Excited	K_{rot}	K_r	τ_i	τ_k
α_2^{1c1}/q	Upper	0.0055	0.22	0.127	1.8
α_2^{1c2}/q	Lower	0.0065	0.24	0.091	1.8
α_2^{1s1}/p	Upper	0.0035	0.28	0.172	1.7
α_2^{1s2}/p	Lower	0.0033	0.26	0.164	1.5

Table 3: Identified K_{rot} factors and time constants for the generic co-axial rotor at 40 knots

Frequency Response	Rotor Excited	K_{rot}	K_r	τ_i	τ_k
α_2^{1c1}/q	Upper	0.0045	0.11	0.024	1.6
α_2^{1c2}/q	Lower	0.0084	0.14	0.002	1.8
α_2^{1s1}/p	Upper	0.0065	0.18	0.144	1.5
α_2^{1s2}/p	Lower	0.0051	0.17	0.196	1.3

Using Equation 4 and L as identified for each flight condition, the traditional wake distortion factor K_r (Ref. [17]) is also presented in these tables. The identified rotation effect time delay, τ_k, is consistently identified in the 1.3 to 2.1 second range with higher airspeeds tending towards lower time delay. K_{rot} shows a significant decrease moving past hover while the converted K_r value shows a more gradual exponential decay pattern. The trend for K_r with airspeed is better visualized in Figure 13. This agrees with the findings of Refs. [11] and [17], with the notable difference of the magnitude of the factor being smaller. Whereas the single rotor study of Ref. [17] suggests $K_r = 1.5$ as an appropriate value for hover, the values identified by this co-axial rotor study are roughly a quarter as large. This reduction is likely due to canceling between the rotation effects of the close proximity coaxial rotors, but is an area that could use further study.

Integrated Simulation with Co-Axial Rotor Helicopter

The identified inflow model and rotor TPP rotation effect were integrated into a full FLIGHTLAB nonlinear simulation model using table lookup method. The simulation model uses four blade rotors with characteristics as outlined in Table 4 and built using blade element formulation. The rotor induced inflow is modeled using the CIFER-identified inflow parameters by interpolating between the identified flight conditions based on wake skew angle and climb rate. The FLIGHTLAB simulation model includes a control

system consisting of four channel control rigging with SAS feedback on longitudinal, lateral, and directional channels to maintain stability. PID controllers serve as the SAS, and were necessary to maintain the flight condition for the duration of the flight dynamics tests.

Table 4: Co-axial rotor parameters

R	Ω	S_{hub}	C_T	ω_f
30.55 ft	23.7 rad/s	4.28 ft	0.0085	1.5/rev

Additional rotor states were added to the simulation model to accommodate the identified second order TPP rotation effects. Four new states are given to each rotor - two states corresponding to the self-induced effects from pitching rate and rolling rate, and two states to account for the rotor-on-rotor effects for the co-axial interactions. The identified K_{rot} and τ_k are then assigned from the identified values as appropriate for the given flight condition.

Control input frequency sweeps were applied to assess the impacts of the inflow model and TPP rotation effects on the flight dynamic characteristics. A version of the simulation model with VPM inflow was produced to serve as the baseline truth data for the response. The hover condition explored in Ref. [8] was expanded to include the responses of the rotor flapping and inflow states in the frequency domain for the nonlinear model. The emphasis of the study was placed on development of a linear flight dynamics model for control design and stability assessment applications, as this application had not been explored in the previous study. Linearization was performed on the simulation model to verify that the inflow and rotation characteristics are properly captured by the linear time-invariant model. Finally, an investigation of the flight dynamics at 40 knots was performed to assess the TPP rotation effect contribution during transition flight.

Figure 14 illustrates the simulation model's pitch rate frequency response to longitudinal stick sweep, q/x_b, in hover for the model with and without K_r. Due to the rotor blade stiffness and co-axial interactions, the TPP rotation effect noticeably improves the low frequency magnitude match to the VPM target. At the lower frequencies, the larger hub rotations allow more time for the rotation effect to propagate and impact the flight dynamic response. The off-axis response, p/x_b, of Figure 15 shows that the rotation effect off-axis impact was negligible, with both identified models over-approximating the off-axis response while achieving the appropriate sign. Figures 16 and 17 present the responses for the upper rotor cosine inflow state and upper rotor lateral flapping response to further

show how inclusion of the TPP rotation identification improves the inflow model. The improvement to the low frequency range is again most notable.

The hover investigation was further expanded beyond Ref. [8] by assessing the inflow model and TPP rotation effect for the application of a linear time-invariant (LTI) model. Because the LTI model is often more appropriate for performance evaluation and control design, knowing that linearization properly captures the inflow characteristics is of particular importance. The nonlinear model with identified inflow with and without TPP rotation effect was linearized via FLIGHTLAB to obtain linear models of 35 states and 27 states, respectively (8 TPP rotation states, 12 flapping dynamic states, 6 inflow states, and 9 body states were retained). For investigation of the linear time-invariant model, pitch and roll rate responses were obtained for the hover flight condition for both a frequency sweep and doublet control input. Figures 18 and 19 show how the frequency domain response of the linearized model compares to the nonlinear response for the pitch and roll channels. The linear model response closely agrees with the nonlinear model with the identified inflow model and the VPM truth model response. Figures 20 through 23 show the LTI model responses for both the frequency and time domains with and without inclusion of the TPP rotation effect. In both frequency and time domains, the presence of the K_r factor greatly improves the match with the VPM truth model.

Figures 24 and 25 are the longitudinal flight dynamic responses at 40 knots forward flight in the frequency and time domains, respectively. A strong match to VPM with very little change between identified models with and without the rotation parameters suggests that the rotation effect is largely washed out, even at this relatively low flight speed. While only the longitudinal response is shown, a similar trend was experienced in the other control channels. Therefore, one can conclude that inclusion of TPP rotation effect identification is critical for proper inflow modeling of the hover and near hover flight conditions, but rapidly becomes insignificant as airspeed increases. This outcome is thus in agreement with the identification results shown in Tables 1 through 3.

Rotor Interference on Aerodynamic Surfaces

An additional component of the inflow modeling methodology that was expanded through this research was the modeling of the rotor interference on the aerodynamic tail surfaces of the co-axial vehicle. As described by Equations 5 and 6, the effective interference velocity on a particular aerodynamic surface was determined from the rotor inflow states and matrices of gain and time delays identified from VPM simulation data. This section covers the identification of the interference parameters and once again explores impacts on the simulation model flight dynamics for the hover flight condition.

Identification and Verification of Rotor Interference Parameters for Aerodynamic Surfaces

VPM simulation allows for velocity sampling at specified points during runs of the co-axial rotor model, thus interference time histories at the aerodynamic surfaces are generated alongside the inflow state histories during the identification process. Figure 26 and 27 illustrate the rotor wake and sampling points used for data collection for the stabilator and side fins. The chosen sampling points allow for the velocity at the quarter chord of the root, midspan, and tip of each aerodynamic surface to be averaged to better simulate the interference across the span. Figure 28 shows the effective downwash velocity response on the right stabilator collected during a frequency sweep of a uniform thrust excitation of the upper rotor at 80 knots. The response of the gain and time delay identified via CIFER[®] are overlaid to show the excellent fit of the identification. The frequency domain response generated by CIFER[®] and transfer function fitting are presented in Figure 29. The frequency domain cost parameter of $J = 3.7$ indicates essentially perfect model agreement. This process was used to identify parameters to fully fill the matrices of Equation 6 for each surface, offering a more complete interference model than was presented in Ref. [8]. While a majority of the matrix elements were easily identified with fitting costs within the satisfactory threshold, certain off-diagonal parameters were assumed zero due to low coherence and magnitude in the associated frequency response.

Validation with Integrated Co-Axial Vehicle Model for Hover

The flight dynamic responses of the simulation model with identified inflow with and without the rotor interference on aerodynamic surface component were determined and evaluated against the VPM simulation model to validate the impact of the enhancement at hover. In Figures 30 through 33, a Bode plot is provided for longitudinal, lateral, collective, and directional with fitting cost included. In all cases, the cost functions

are $J \leq 100$, indicating satisfactory model accuracy (Ref. [13]). Figures 30 and 31 suggest that the impact of interference at the tail on the pitch and roll response is negligible. Because the tail surfaces are outside the main rotor wake for the hover flight condition, this result is expected. For the heave response to collective (Fig. 32) and the yaw rate response to pedal (Fig. 33), inclusion of the rotor interference did improve the low frequency response a small amount, suggesting that the low frequency excitations of these channels influenced the rotor wake enough to impact the tail surface effectiveness at hover. For both cases, however, the fitting cost is acceptable even without the interference model. To further explore the accuracy of the interference model, the aerodynamic surface interference velocities and forces were collected and evaluated for the hover trim condition. Table 5 presents the collected data for the left stabilator surface. The identified interference model corrects the downwash velocity experienced by the surface as well as the resulting aerodynamic force. Similar improvement was seen in the right stabilator and vertical fins.

Table 5: Aerodynamic characteristics of the left stabilator at hover trim

	VPM	ID with Interference	ID without Interference
Downwash	19.3 ft/s	18.0 ft/s	0 ft/s
Download	12.2 lbs	12.2 lbs	0 lbs

This investigation of the rotor interference on aerodynamic surface model reveals that the established identification process improves simulation of the surface velocities and forces, with minor improvements to the overall flight dynamics simulation at hover. Exploration of the interference on aerodynamic surface effects in forward flight found noticeable influence on the vehicle trim while evaluation of its impact on vehicle dynamic response is ongoing and thus not presented.

Rotor Interference on Fuselage

This section covers the identification and verification of parameters used to model the rotor interference on the fuselage, then discusses the impacts on the full vehicle flight dynamics. Focus is placed on the multi-point sampling method developed to better approximate the averaged interference effect.

Identification and Verification of Rotor Interference Parameters for Fuselage

The rotor interference on fuselage again uses the formulation established in Equations 5 and 6, where the interference velocity is modeled from each rotor's inflow states using interference matrices of gain and time delays identified from VPM simulation using CIFER®. Figure 34 illustrates this modeling scheme by showing the data flow from the rotor inflow states to the fuselage airloads. In the studies performed in Ref. [8], the interference velocity sampled at the vehicle C.G. was used in parameter identification. As Figure 35 shows, the experienced interference velocity varies significantly with location on the fuselage, thus identification from a single point is likely an unreliable representation of the fuselage as a whole. As such, an effective interference velocity was determined by weighted average of a series of sample points spanning the surface of the fuselage. Figure 36 shows the fuselage geometry and points selected for interference velocity sampling, while Equation 7 provides the formulation for the effective interference velocity. The six fuselage points chosen cover the major regions of the fuselage while maintaining a small sample set for simplicity. A weighting factor based on sample point offset from the moment center is included to better model the interference effect on fuselage moments. Figure 37 shows an example gain and time delay identification fitting to a frequency response of the effective interference velocity from six sample points during VPM simulation. A good fit is achieved, showing that the averaging scheme does not degrade the identification quality. Table 6 presents the identified gains and associated costs for the hover flight condition to show that a precise identification model ($J < 30$) is achieved for the parameters of the inflow states with a direct impact on downwash.

Table 6: Interference matrix elements identified from the weighted average interference velocity, hover

Input	Output	Gain	Time Delay (ms)	Cost
α_1^{0c1}	w	-2.49	40.7	19.3
α_2^{1c1}	w	-3.08	154.9	19.8
α_2^{1s1}	w	0	0	-
α_1^{0c2}	w	-2.52	24.6	12.6
α_2^{1c2}	w	-1.88	34.8	28.9
α_2^{1s2}	w	0	0	-

Table 7: Force and error comparison for various fuselage interference approximation methods, hover

	Single Point (C.G.)	Algebraic Average	Offset Weighted Average	VPM-CFD Target
w_i [ft/s]	-66.8	-59.7	-78.0	
$\tilde{D}$ [lbs]	1575.9	1257.2	2079.6	2073.5
ϵ_a [lbs]	497.6	816.3	6.1	
ϵ_r [%]	24.0	39.4	0.29	
$\tilde{L}$ [lbs]	52.9	42.2	71.7	76.0
ϵ_a [lbs]	23.1	33.8	4.3	
ϵ_r [%]	30.4	44.5	5.6	
$\tilde{M}$ [ft-lbs]	7926	5068	11310	12325
ϵ_a [ft-lbs]	4399	7257	1015	
ϵ_r [%]	35.7	58.9	8.2	

Validation with Integrated Co-Axial Vehicle Model for Hover and 80 Knots

The identified interference matrices for rotor interference on fuselage were incorporated into the co-axial simulation model as table lookup values. Prior to running flight dynamic analysis, the trim fuselage forces and moments were determined for several interference modeling options and flight conditions. Table 7 presents the hover comparison between identified interference from velocity at a single point at the C.G., from an algebraic average velocity of the six sample points, and from the offset weighted average velocity determined from Equation 7. The comparison of trim force and moment outputs shows that the offset weighted formulation significantly improves the simulation of the fuselage characteristics.

The rotor interference on fuselage effects on the flight dynamics were then assessed with Figures 38 through 40 covering the hover flight condition. The identified inflow model without rotor interference on fuselage, with single point interference on fuselage, and with 6 point offset weighted interference on fuselage are compared. The main impact is seen in collective response (Fig. 40) where the 6 point average interference on fuselage shows a better fit throughout the low and mid frequency ranges. To better visualize this improvement, Figure 41 plots the error between each identified model option and the VPM baseline. The 6 point average improves the maximum magnitude error by roughly 1 dB (12%) over the other interference options for a majority of the 0.5 - 20 rad/sec frequency range.

Next, a similar investigation was performed at 80 knots to assess the forward flight characteristics. At this airspeed, the longitudinal 42), lateral (Fig. 43), and collective (Fig. 44) channels each show negligible influence from the rotor interference on fuselage while maintaining a satisfactory fit to the VPM simulation.

At 80 knots, the fuselage is largely outside the wake produced by the rotors, thus the lack of significant influence is expected. Figure 45 is included to show that some improvement in the heave response in the time domain was recorded - the initial acceleration spike to a collective doublet was best modeled with the 6 point interference approach. However, this improvement is very small and each of the identified models shows an acceptable time domain response.

The main conclusion derived from this rotor interference on fuselage analysis is that the interference effect is most noticeable at hover and in the heave channel, but contributes less to the overall flight dynamics than the core inflow dynamics or the rotor TPP rotation effect. Interference identification may be needed to properly model heave flight dynamics and is very important in properly predicting the trim fuselage aerodynamic loads, in which case sampling multiple points improves the model considerably.

Impact on Flight Dynamics and Control Design

As a final investigation of the overall impact of the inflow identification process on co-axial vehicle modeling and design, a comparison of the broken-loop responses and associated stability margins was conducted between the tradition Peters-He three state inflow model and the identified inflow model. The simulation model with identified inflow includes the TPP rotation effect and interference models to assess the complete identification technique studied in this paper. The simulation model coupled with VPM inflow is again run for the same condition to serve as the truth data for response and margin comparison. The broken-loop Bode plots (Ref. [21]) and stability margins for select control channels at

hover and 80 knots are included to show the advantages of the identified inflow model over the Peters-He inflow model.

A simplified block diagram of the co-axial vehicle control system is shown in Figure 46. Stability is maintained through the PID controller feedback of the SAS. The broken-loop response was determined by evaluating the output of the SAS, $f(s)$, for a given input to the airframe, $e(s)$.

The lateral broken-loop response (Fig. 47) shows considerable improvement in cost as well as improved match in stability margin values. Table 8 shows that both the gain and phase margin for the identified inflow model accurately reflects the control characteristics of the VPM model, whereas using the Peters-He inflow model yields overly optimistic margins.

Table 8: Stability margins for lateral channel, hover

	VPM	Identified Model	Peters-He
ω_G [rad/s]	1.83	2.06	1.03
ω_{180} [rad/s]	27.3	27.4	27.7
G.M. [dB]	7.55	7.10	8.57
P.M. [deg]	137.0	138.5	162.2

The heave broken-loop response (Fig. 48) and stability margins (Table 9) reflect these trends, with both gain and phase margin showing better match to VPM with the identified model due to the response magnitude being much more similar to the VPM values.

Table 9: Stability margins for collective channel, hover

	VPM	Identified Model	Peters-He
ω_G [rad/s]	2.67	2.54	3.53
ω_{180} [rad/s]	27.7	28.8	28.1
G.M. [dB]	6.24	6.46	7.10
P.M. [deg]	90.6	92.8	98.4

One response was also included to show the improvements for forward flight. The longitudinal response at 80 knots, shown in Figure 49, again shows a notable reduction in cost with the adoption of the identified inflow model, although the improvement is not as extreme as in hover. For stability margins (Table 10), the Peters-He model shows the largest gain margin overprediction thus far whereas the identified inflow model very accurately predicts this margin.

These frequency response and stability margin assessments show that the traditional Peters-He inflow model is insufficient for use in multi-rotor applications. Meanwhile the identified inflow model methodology accomplishes the goal of capturing the multi-rotor inflow characteristics important in flight dynamic and

Table 10: Stability margins for longitudinal channel, 80 knots

	VPM	Identified Model	Peters-He
ω_G [rad/s]	3.34	4.07	4.68
ω_{180} [rad/s]	20.4	17.7	20.9
G.M. [dB]	9.53	9.62	12.21
P.M. [deg]	118.7	114.4	115.3

control design while retaining a state space form that is consistent with all existing real time full flight simulation formulation for an easy implementation.

Summary and Conclusions

A state space inflow model determined through CIFER$^{\circledR}$ identification from Viscous Vortex Particle Method simulation was evaluated and verified for a co-axial rotor configuration and enhanced through inclusion of models for rotor TPP rotation effect and rotor interference on fuselage and aerodynamic surfaces. From the simulation research performed to verify the identification methodology with these enhancements, the following conclusions are made:

1. The identification methodology covers the inflow model, mutual interference between rotors, TPP rotation effect, and interference on other airframe components in a unified formulation structure.

2. The identification method is robust and achieves low cost fits, resulting in state space models for inflow and interference that are suitable for multi-rotor air vehicle control design and analysis.

3. The TPP rotation effect is well captured via gain and time delay identification from rotation excitation of the VPM coupled rotor model. Inclusion of this effect in the inflow dynamics greatly improves the hover flight dynamics response of the simulation vehicle, but becomes less significant with increasing airspeed. Identified K_r values for the co-axial rotor are less than those used for a single articulated rotor.

4. Rotor interference on fuselage and aerodynamic surfaces is well captured and has notable impact for certain responses and flight conditions. Using multiple sample points to determine the interference velocity on the fuselage improves simulation of forces and moments and increases the accuracy of the heave response.

5. Adopting the identified inflow model significantly

improves the accuracy of flight dynamics response and stability margins over the Peters-He model, and is thus much more suitable for FVL applications.

These findings were verified through flight dynamic analysis of the identified inflow model in comparison to VPM simulation. For the co-axial configuration considered, the identified inflow model achieved an excellent match for all controls channels at several airspeeds, supporting the conclusion that the identification methodology is the appropriate choice for multi-rotor simulation.

Acknowledgment

References

[1] Pitt, M. and Peters, A.,"Dynamic Inflow for Practical Applications," Vertica, Vol.5,(1), 1981.

[2] Peters, D. A. and He, Chengjian,"Finite State Induced Flow Models Part II: Three Dimensional Rotor Disk," *Journal of Aircraft*, Vol. 32, No. 2, March-April, 1995, pp. 323-333.

[3] Nowak, M.; Prasad, J.V.R. and Peters, D.A., "Development of a Finite State Model for a Coaxial Rotor in Forward Flight," AHS 70th Annual Forum, Montreal, Quebec, Canada, May 2014.

[4] Xin, H., Goss, J. D., and Parkes, C., "Development of a Three-State Rotor Interference Model and Application to Coaxial Rotor Inflow Modeling, AHS Specialists Conference, SF, CA, Jan. 2014.

[5] Gunner, F.; Yong-Boon, K., Prasad, JVR.; Peters, D.; and C. He, "Development of a Finite State Dynamic Inflow Model for Multi-Rotor Configurations using Analytical Approach, 74th AHS Annual Forum, May 2018.

[6] Rand, O; Khromov, V.; Hersey, S.; Celi, R.; Juhasz, O.; and Tischler, M.,"Linear Inflow Model Extraction from High-Fidelity Aerodynamic Models for Flight Dynamics Applications," AHS 71st Annual Forum, Virginia Beach, VA, May 2015.

[7] He, Chengjian; Syal, M.; Tischler, M.B. and Juhasz, Ondrej, "State-Space Inflow Model Identification from Viscous Vortex Particle Method for Advanced Rotorcraft Configurations," AHS 73rd Annual Forum, Fort Worth, TX, May 2017.

[8] He, Chengjian; Gladfelter, M.; Chang, C.; Tischler, M.B. and Juhasz, Ondrej, "VPM-Derived State Space Inflow Model for Multi-Rotor Air Vehicle Modeling and Simulation," VFS 75rd Annual Forum, Philadelphia, PA, May 2019.

[9] Hersey, Sean and Juhasz, Ondrej,"Accurate State-Space Inflow Modeling for Flight Dynamics and Control of a Coaxial-Pusher Rotorcraft," AHS 74th Annual Forum, Phoenix, AZ, May 2018.

[10] Keller, J. D.; McKillip, R. M.; Wachspress, D. A.; Tischler, M. B., and Juhasz, O., "A Free Wake Linear Inflow Model Extraction Procedure for Rotorcraft Analysis, AHS 73rd Annual Forum, May 2017.

[11] Keller, Jeffrey; McKillip, Robert; Wachspress, Daniel; Tischler, M.B. and Juhasz, Ondrej, "Linearized Inflow and Interference Models from High Fidelity Free Wake Analysis for Modern Rotorcraft Configurations," VFS 75rd Annual Forum, Philadelphia, PA, May 2019.

[12] He, Chengjian and Rajmohan, N., "Modeling the Aerodynamic Interaction of Multiple Rotor Vehicles and Compound Rotorcraft with Viscous Vortex Particle Method," AHS 72nd Annual Forum, West Palm Beach, May 2016.

[13] Tischler, M.B. and Remple, R.K., *Aircraft and Rotorcraft System Identification*, 2nd Edition, AIAA, Education Series, 2012.

[14] Tischler, Mark B.,"Identification of Bearingless Main Rotor Dynamic Characteristics from Frequency-Response Wind-Tunnel Test Data," *Journal of the American Helicopter Society*, Vol. 44, (1), March-April 1999, pp. 63-76. DOI: 10.4050/JAHS.44.63.

[15] Keller, Jeffrey D. and Curtiss, H. C., "A Critical Examination of the Methods to Improve the Off-Axis Response Prediction of Helicopters," AHS 54th Annual Forum, Washington D.C., May 1998.

[16] Curtiss, H. C., "Aerodynamic Models and the Off-Axis Response," AHS 55th Annual Forum, Montreal, May 1999.

[17] Keller, Jeffrey D. "The Effect of Rotor Motion on the Induced Velocity in Predicting the Response of Rotorcraft," Ph.D. Thesis, Princeton University, Jan. 1998.

[18] Curtiss, H. C. and Quackenbush, T. R. "The Influence of the Rotor Wake on Rotorcraft Stability and Control," Fifteenth European Rotorcraft Forum, Amsterdam, Sept. 1989.

[19] Du Val, R. and He, Chengjian,"FLIGHTLAB Modeling for Real-Time Simulation Applications," International Journal of Modeling, Simulation, and Scientific Computing, Vol. 8, No. 4, 2017.

[20] Johnson, W.; Moddie, A. and Yeo, H.,"Design and Performance of Lift-Offset Rotorcraft for Short-Haul Missions, AHS FVL Conference, SF, CA, Jan. 2012

[21] Tischler, M.B., Berger, T., Ivler, C.M., Mansur, M.H., Cheung, K.K., and Soong, J.Y., *Practical Methods for Aircraft and Rotorcraft Flight Control Design: An Optimization-Based Approach*, AIAA, Education Series, 2017, Chapter 5.
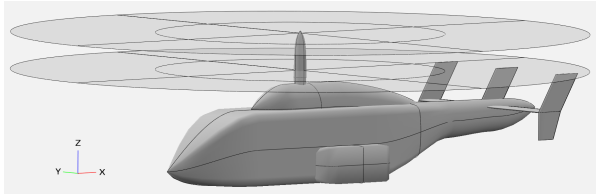
Figure 1: Generic co-axial helicopter model configuration
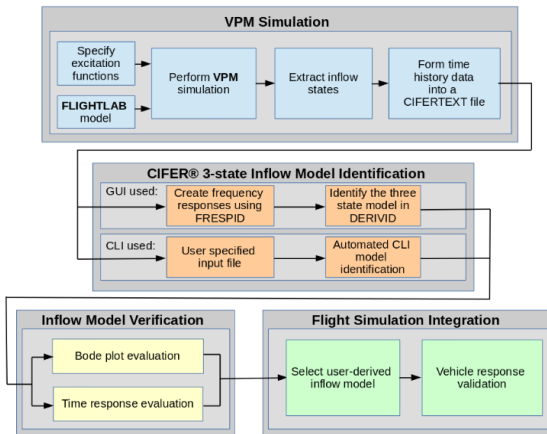
Figure 2: Identification methodology work flow chart
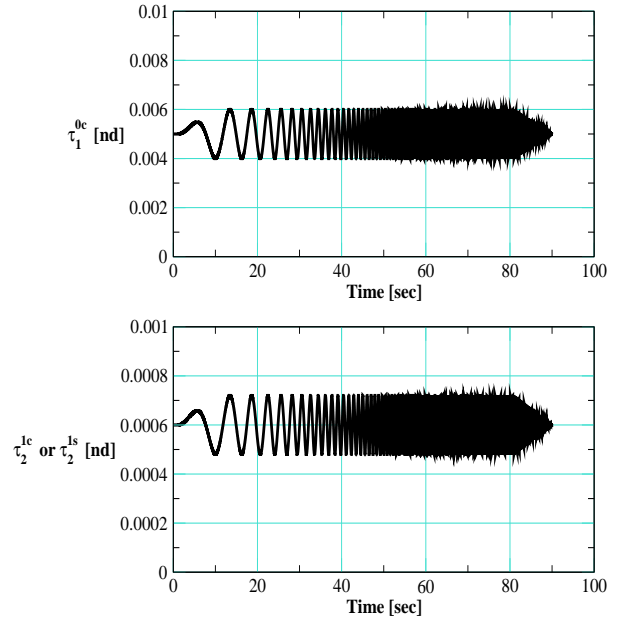
Figure 3: Inflow forcing function excitations applied to a rotor for inflow state model identification
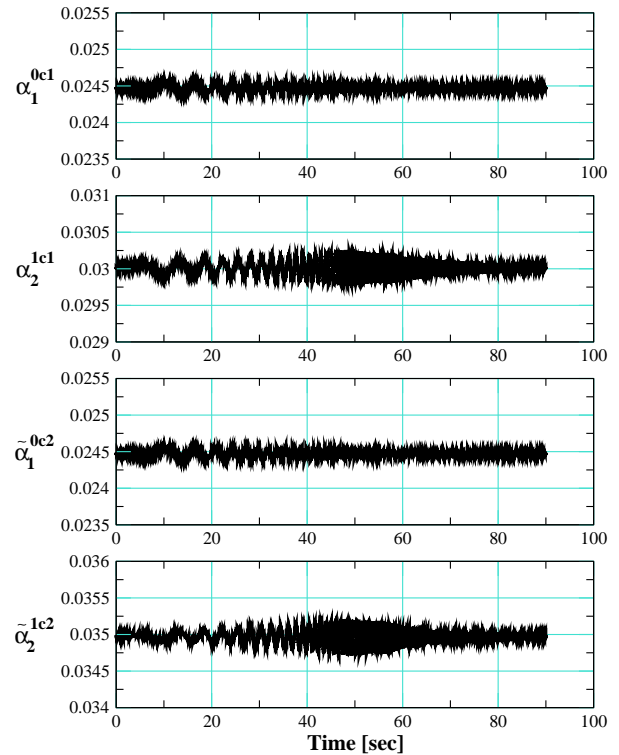
Figure 4: VPM derived upper and lower rotor inflow response to excitation of a hub pitch moment based inflow forcing function ((τ_2^{1c1}) at 40 knots
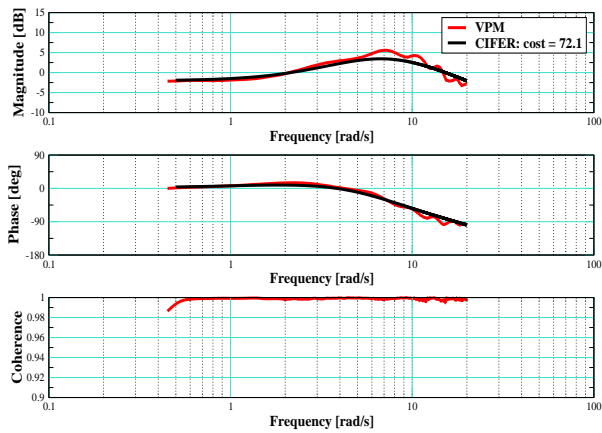
Figure 5: Upper rotor cosine inflow state (α_2^{1c1}) response to excitation of a hub pitch moment based inflow forcing function (τ_2^{1c1}) at 40 knots
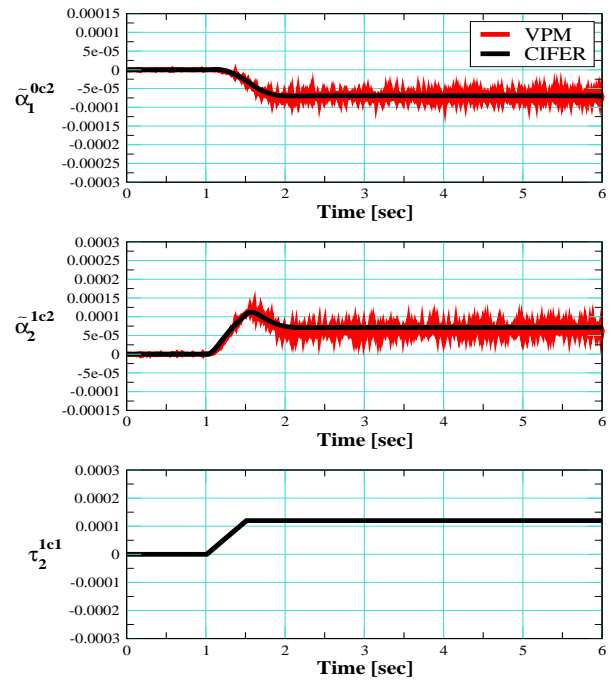
Figure 7: Time domain verification of lower rotor inflow state interference expansion coefficients at 40 knots
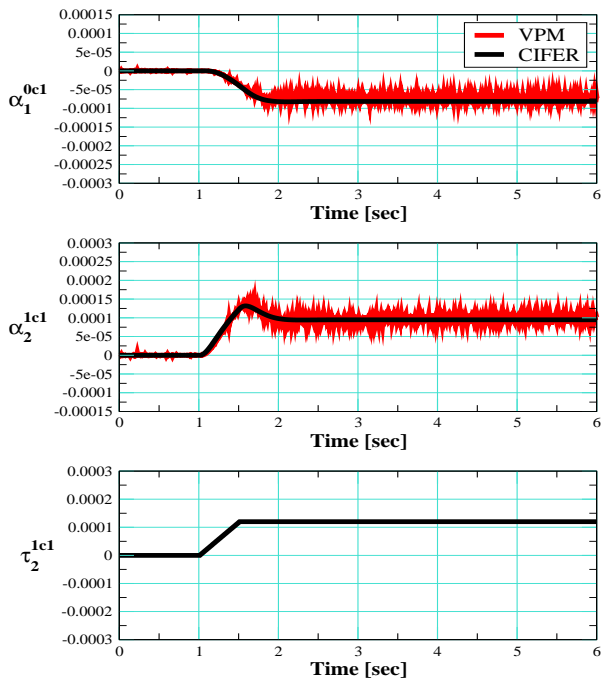
Figure 6: Time domain verification of upper rotor inflow states at 40 knots
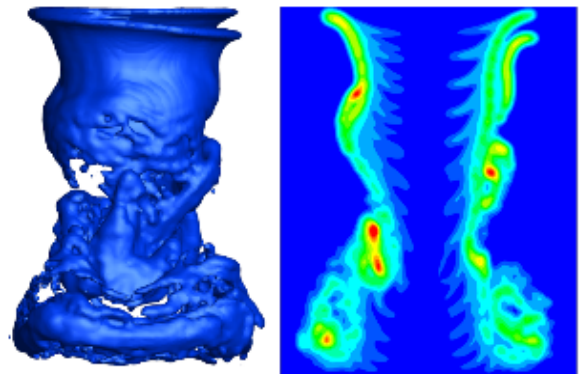
Figure 8: A snapshot of VPM rotor wake (left sideview) showing the wake distortion due to the lower rotor TPP rotation at hover
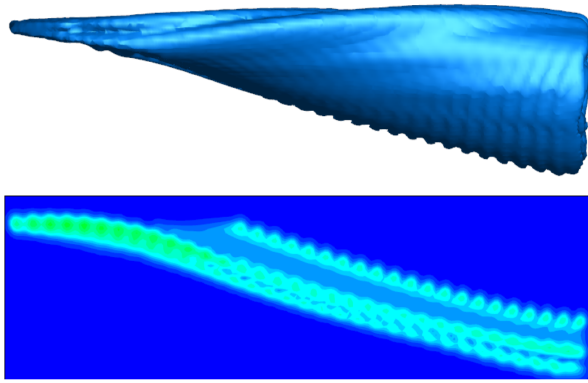
Figure 9: A snapshot of VPM rotor wake (left sideview) showing the wake distortion due to the lower rotor TPP rotation at 40 knots
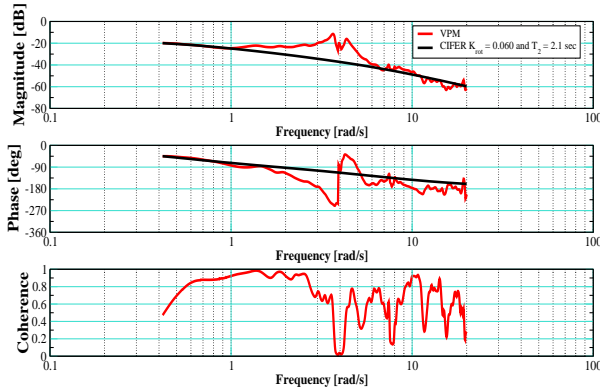
Figure 10: α_2^{1c2}/q transfer function fit at hover
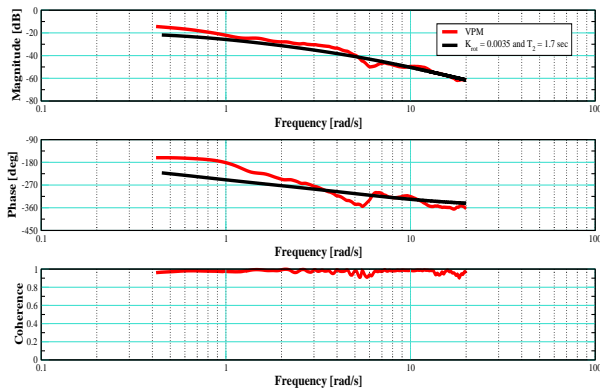
Figure 11: α_2^{1s1}/p transfer function fit at 15 knots
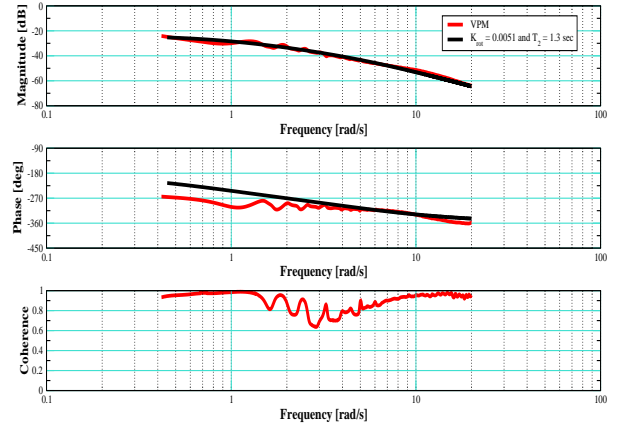
Figure 12: α_2^{1s2}/p transfer function fit at 40 knots
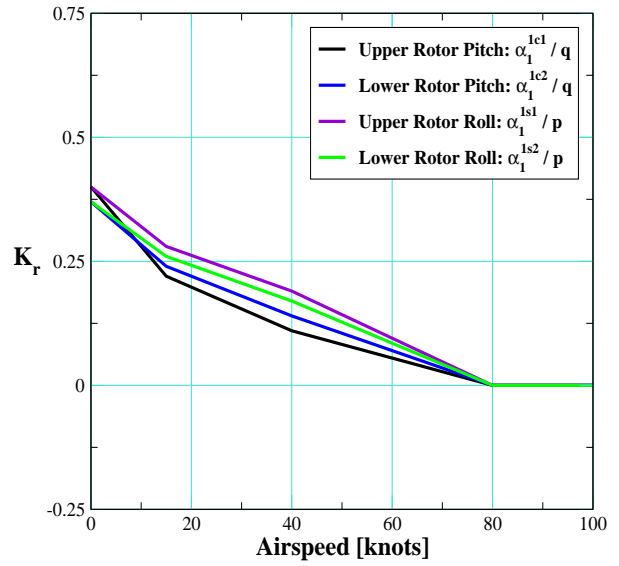
Figure 13: Identified K_r factors as a function of airspeed
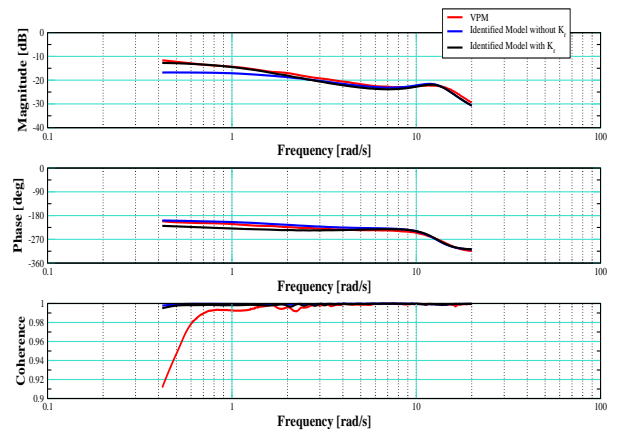
Figure 14: Co-axial nonlinear model pitch rate response to a longitudinal frequency sweep at hover, q/x_b
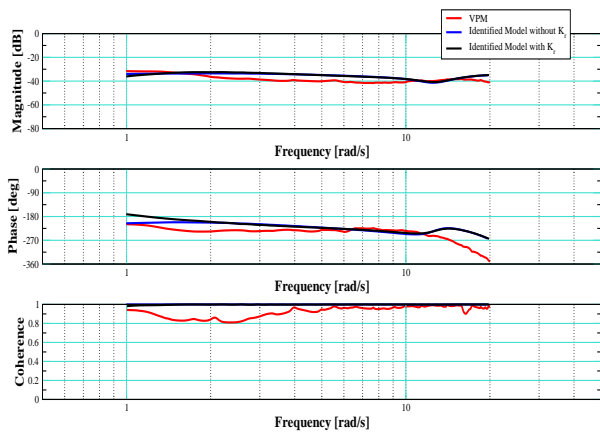
Figure 15: Co-axial nonlinear model roll rate off-axis response to a longitudinal frequency sweep at hover, p/x_b
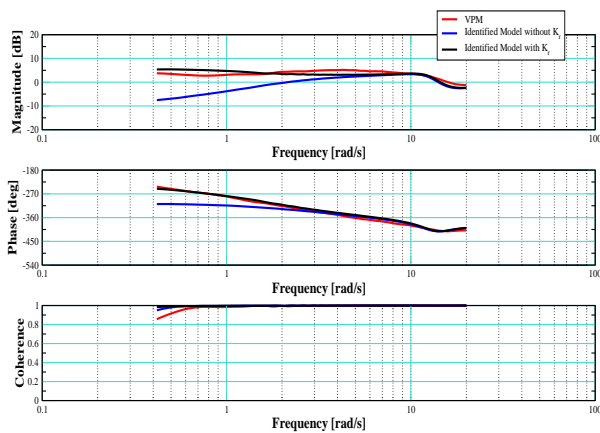
Figure 16: Co-axial nonlinear model upper rotor cosine inflow state response to a longitudinal frequency sweep at hover, α_2^{1c1}/x_b
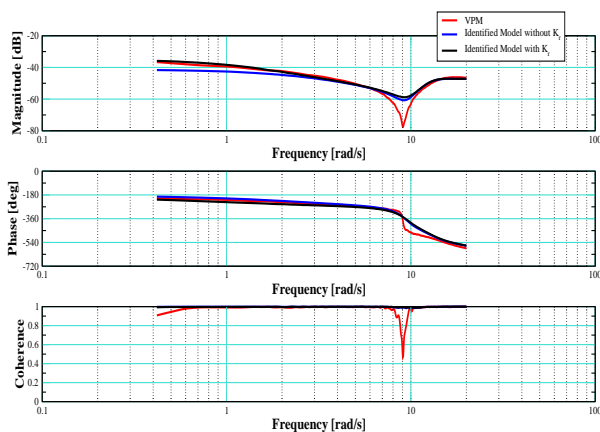
Figure 17: Co-axial nonlinear model upper rotor flapping response to a longitudinal frequency sweep at hover, β_{1s}^1/x_b
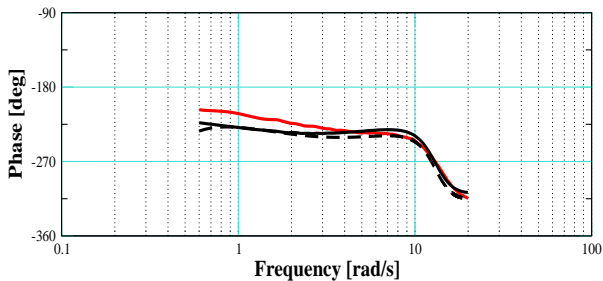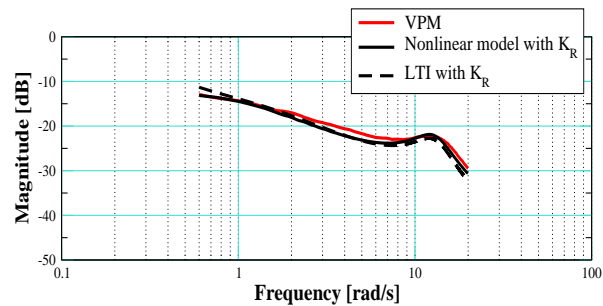
Figure 18: Nonlinear and linear flight dynamics model pitch rate frequency response with TPP rotation effect at hover, q/x_b
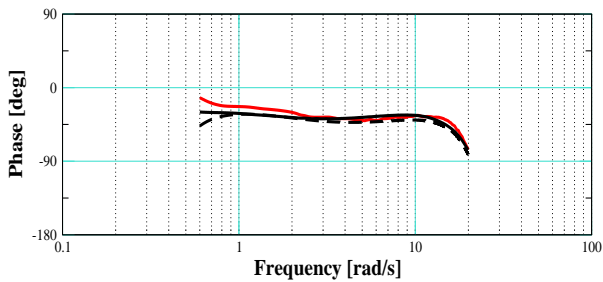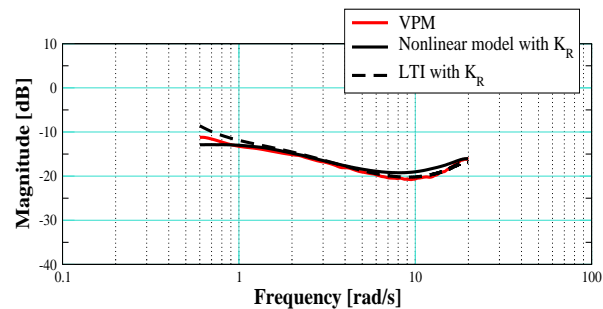
Figure 19: Nonlinear and linear flight dynamics model roll rate frequency response with TPP rotation effect at hover, p/x_a
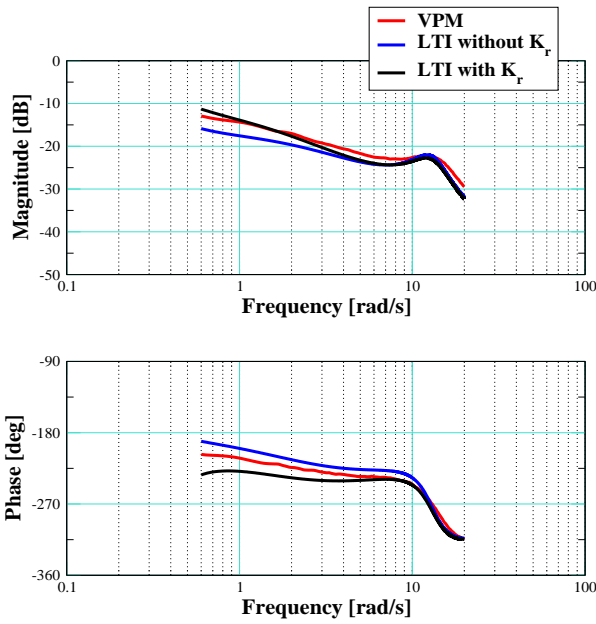
Figure 20: Linear flight dynamics model pitch rate response with and without TPP rotation effect at hover, q/x_b
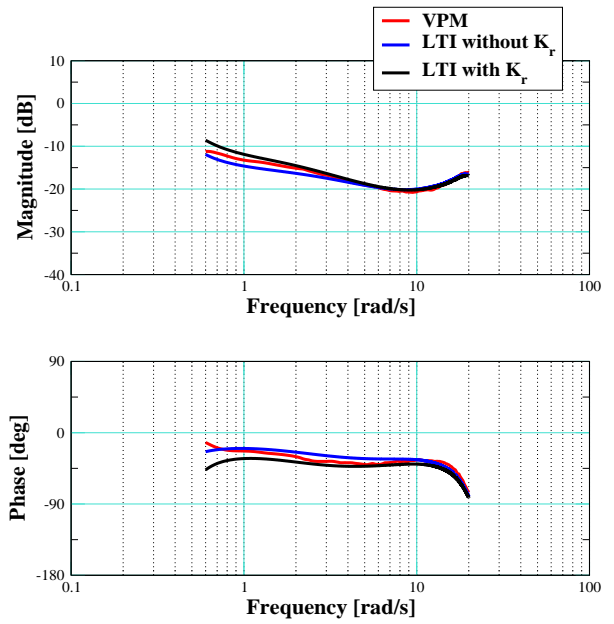
Figure 22: Linear flight dynamics model roll rate response with and without TPP rotation effect at hover, p/x_a
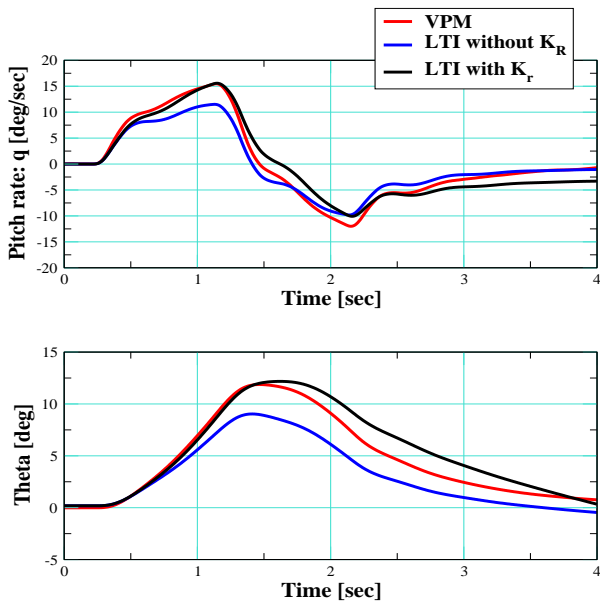
Figure 21: Linear flight dynamics model pitch rate and angle time domain response with and without TPP rotation effect at hover, q/x_b
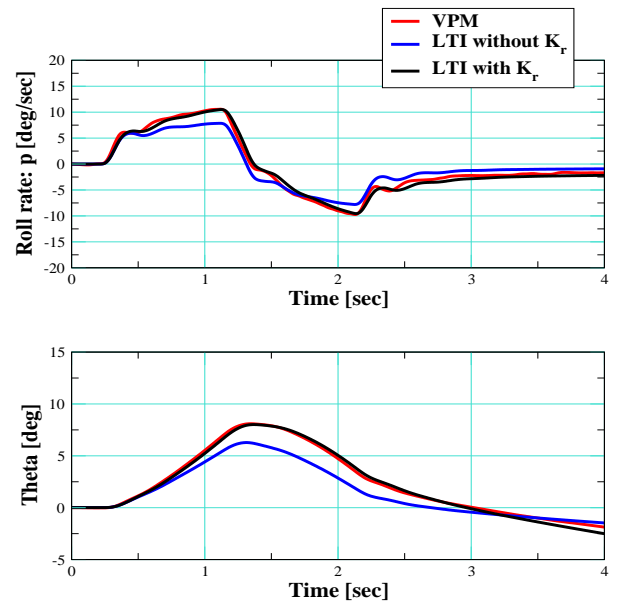
Figure 23: Linear flight dynamics model time domain roll rate response with and without TPP rotation effect at hover, p/x_a
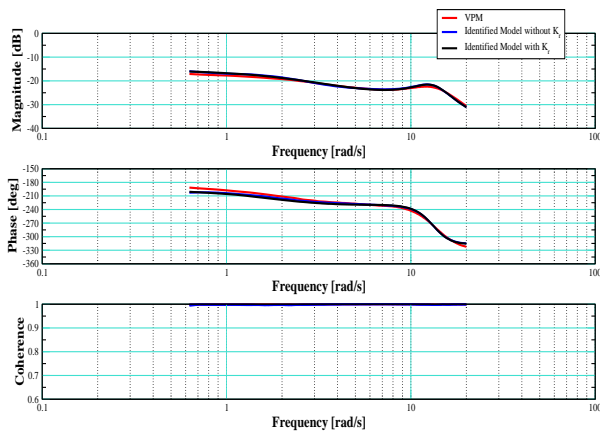
Figure 24: Co-axial nonlinear model pitch rate response to a longitudinal frequency sweep at 40 knots, q/x_b
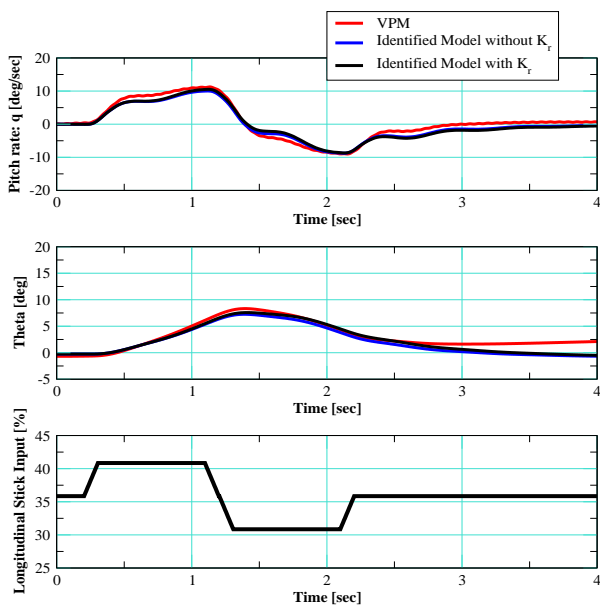
Figure 25: Co-axial nonlinear model pitch rate and angle response to a longitudinal doublet at 40 knots, q/x_b

Sliced at y = 10 ft to pass through right vertical fin points
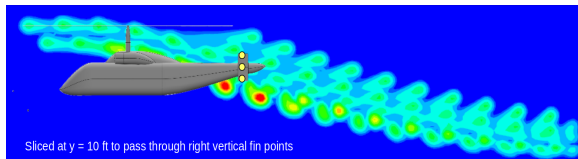
Figure 26: VPM wake Y-plane slice with vertical fin sampling point locations, 80 knots

Sliced at x = 32 ft to pass through empennage points
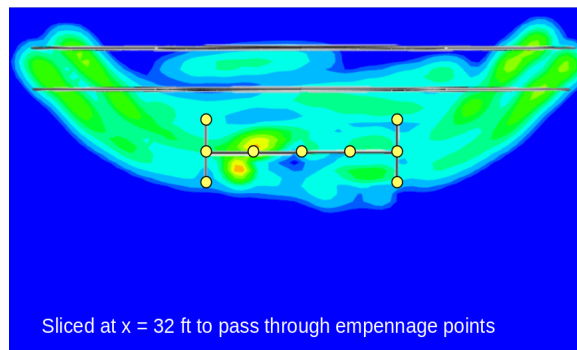
Figure 27: VPM wake X-plane slice with empennage sampling point locations, 80 knots
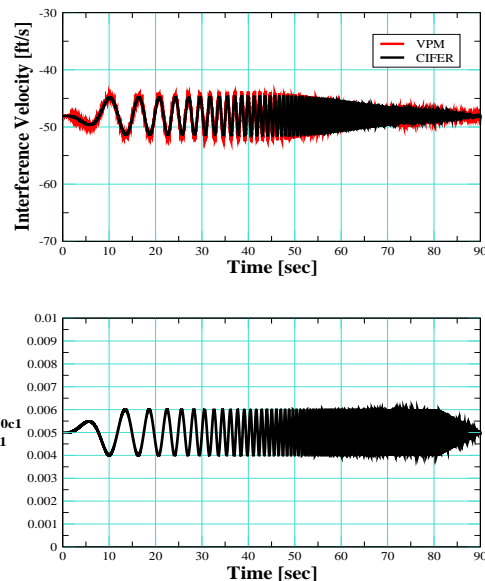
Figure 28: Upper rotor interference velocity on right stabilizer at 80 knots
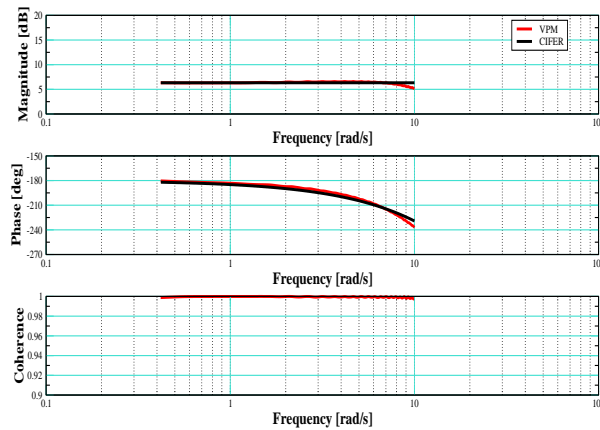
Figure 29: Gain and time delay fitting for the response of the upper rotor interference velocity on right stabilizer at hover, w_z/α_1^{0c1}, fitting cost = 3.7
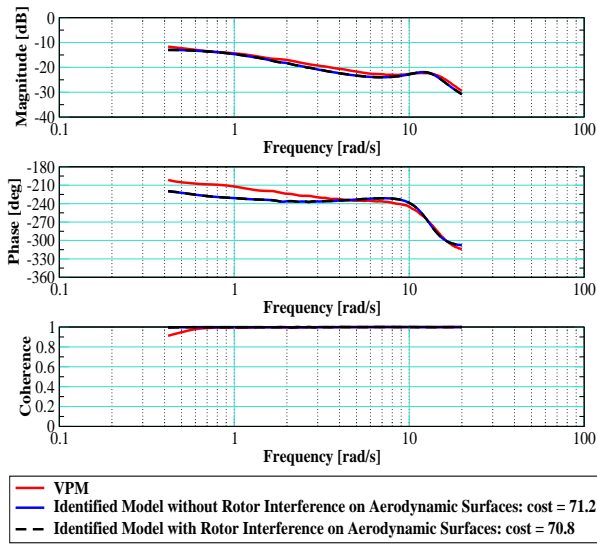
Figure 30: Co-axial vehicle pitch rate response to a longitudinal frequency sweep at hover, q/x_b
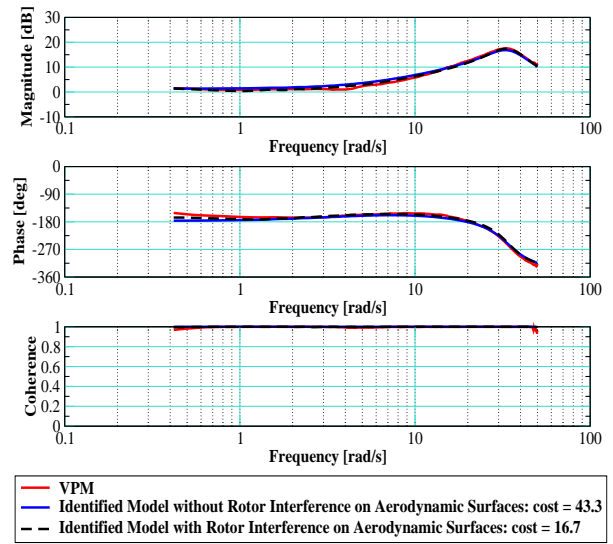
Figure 32: Co-axial vehicle heave response to a collective frequency sweep at hover, Azi/x_c
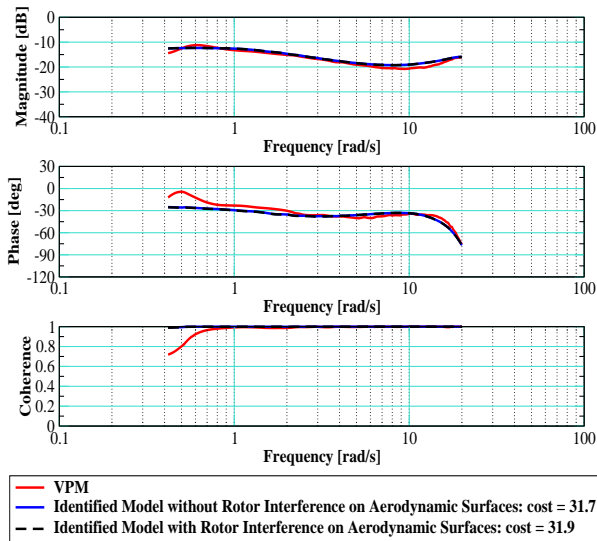
Figure 31: Co-axial vehicle roll rate response to a lateral frequency sweep at hover, p/x_a
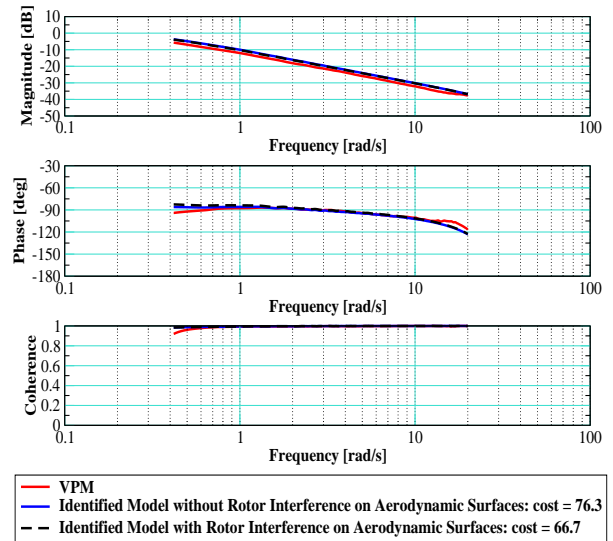
Figure 33: Co-axial vehicle yaw rate response to a pedal frequency sweep at hover, r/x_p
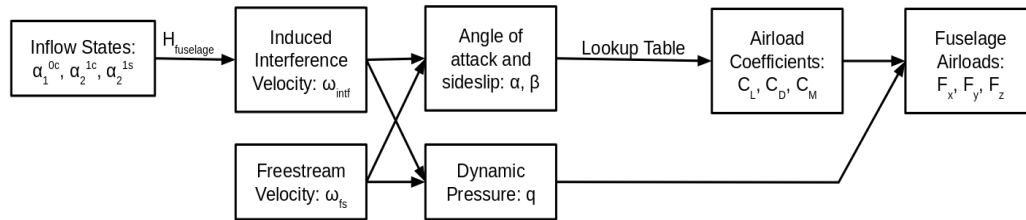
Figure 34: Data flow from rotor inflow states to fuselage forces and moments
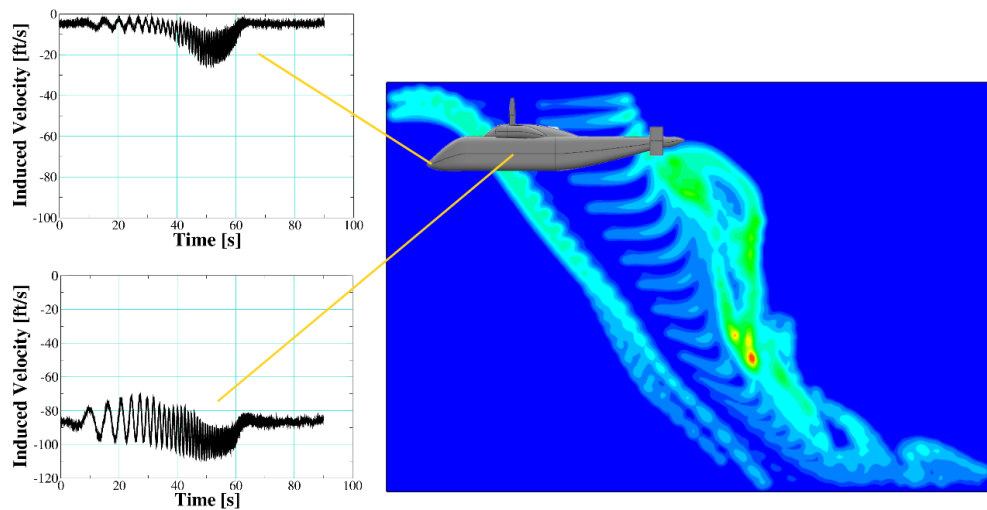
Figure 35: Variation in rotor interference velocity with location on fuselage surface at 20 knots forward flight
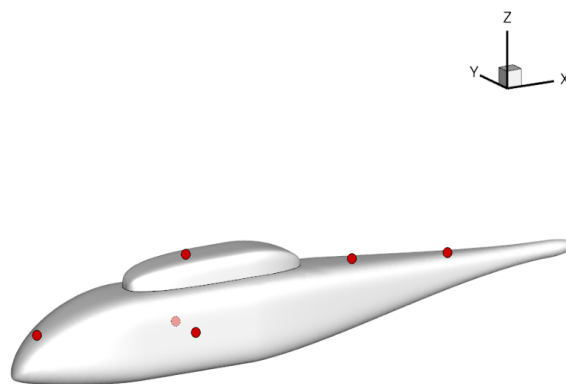
Figure 36: Co-axial vehicle fuselage geometry with locations of interference sampling points
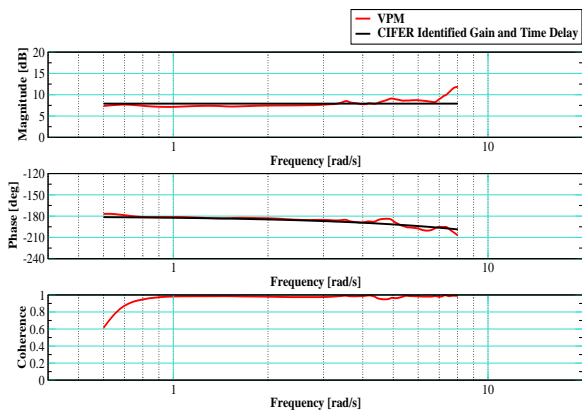
Figure 37: Example gain and time delay fitting for downwash response to upper rotor uniform inflow state, w/α_1^{0c1} [ft/s], for the effective rotor interference velocity on the fuselage
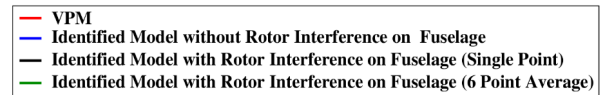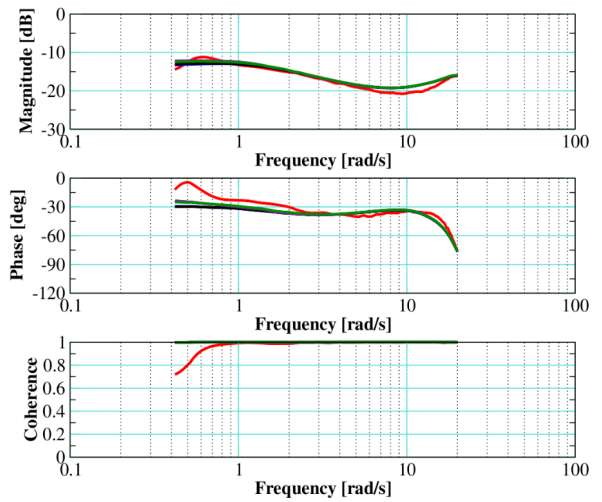
Figure 39: Co-axial vehicle roll rate response to a lateral frequency sweep at hover, p/x_a
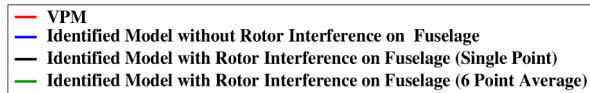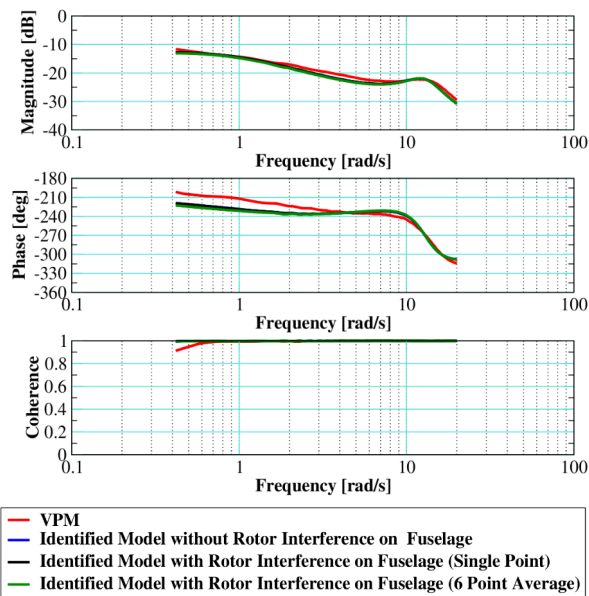
Figure 38: Co-axial vehicle pitch rate response to a longitudinal frequency sweep at hover, q/x_b
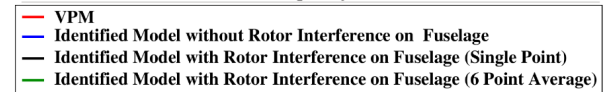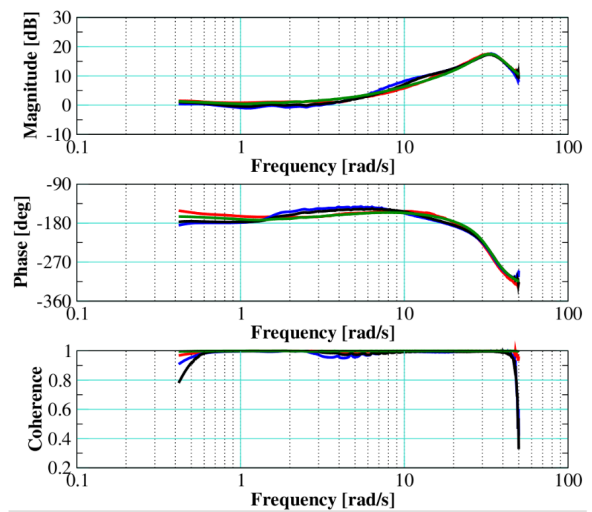
Figure 40: Co-axial vehicle heave response to a collective frequency sweep at hover, Azi/x_c
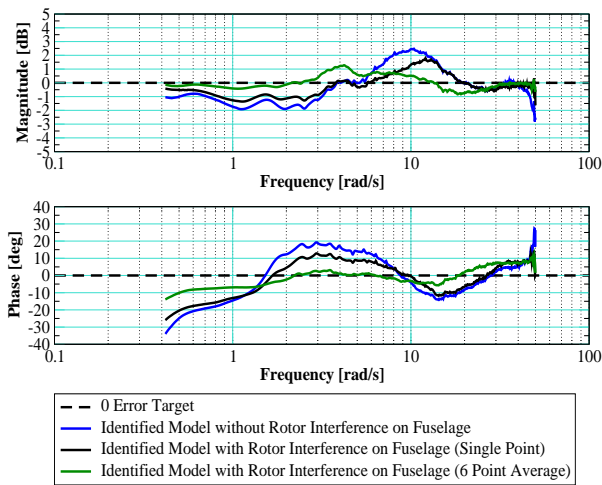
Figure 41: Error in co-axial vehicle identified model heave response at hover compared to VPM, Azi/x_c
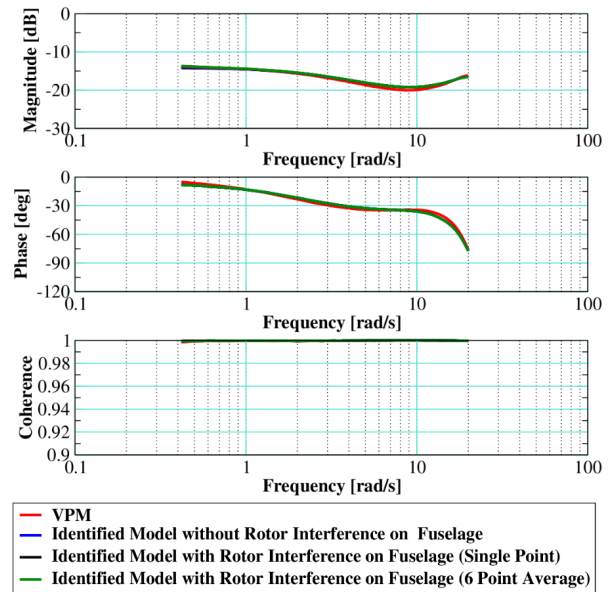
Figure 43: Co-axial vehicle roll rate response to a lateral frequency sweep at 80 knots, p/x_a
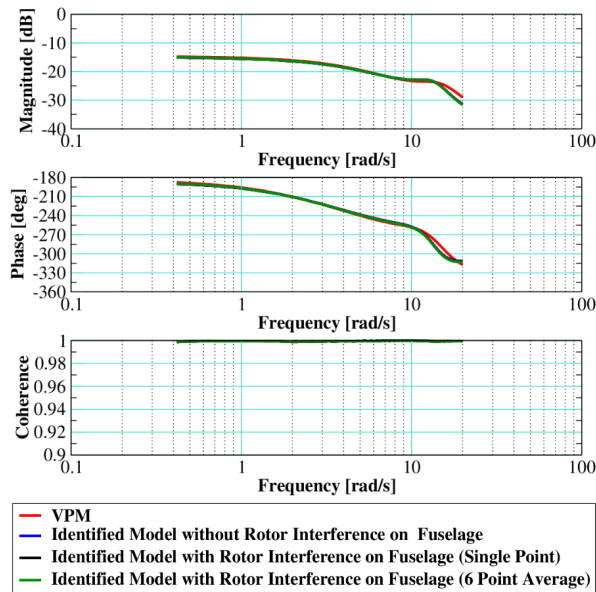
Figure 42: Co-axial vehicle pitch rate response to a longitudinal frequency sweep at 80 knots, q/x_b
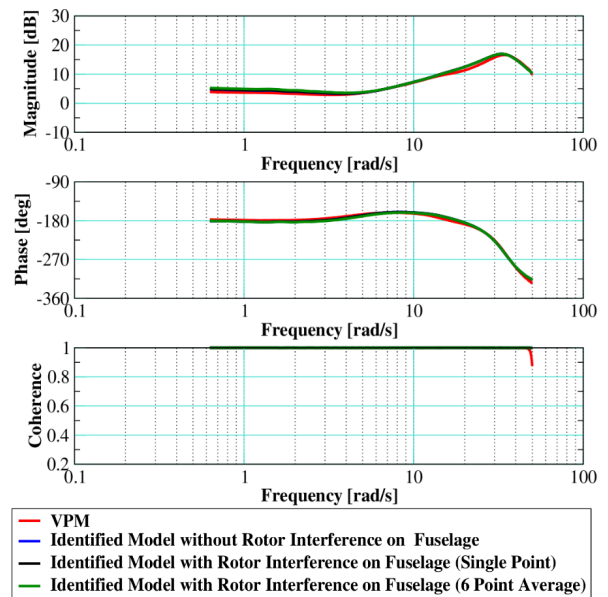
Figure 44: Co-axial vehicle heave response to a collective frequency sweep at 80 knots, Azi/x_c
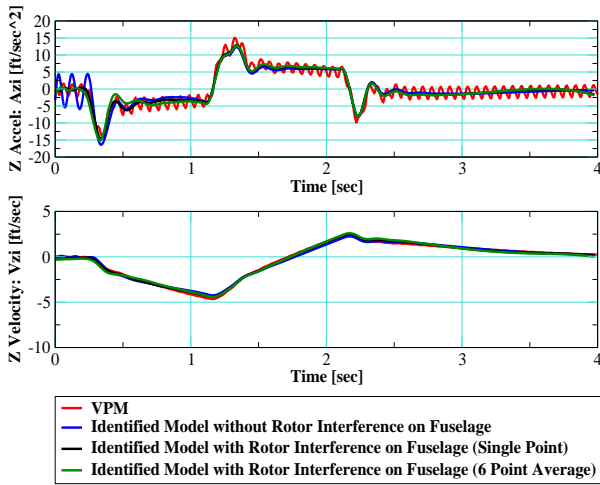
Figure 45: Co-axial vehicle heave response to a collective doublet at 80 knots, Azi/x_c
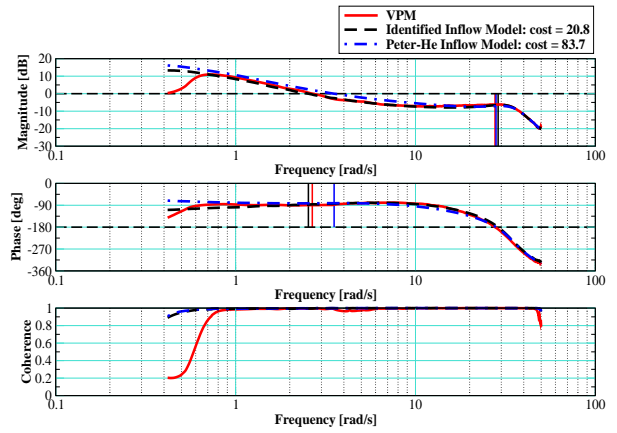
Figure 48: Stability margin assessment of the broken-loop response, $f(s)/e(s)$, for the collective channel, hover
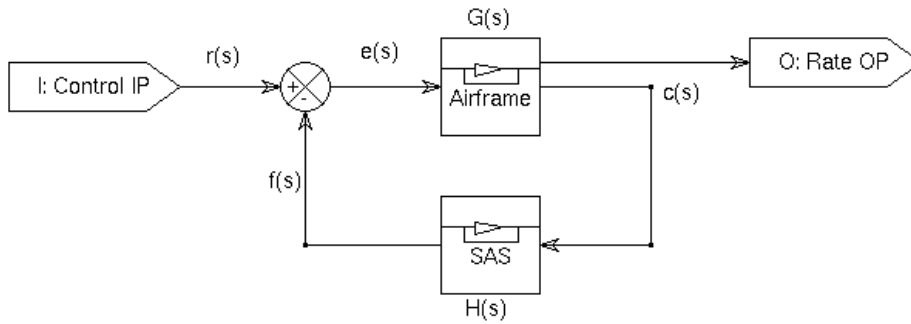
Figure 46: Simplified co-axial vehicle control block diagram
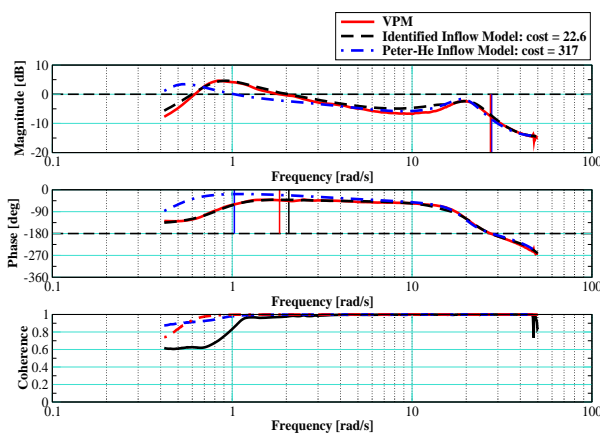
Figure 47: Stability margin assessment of the broken-loop response, $f(s)/e(s)$, for the lateral channel, hover
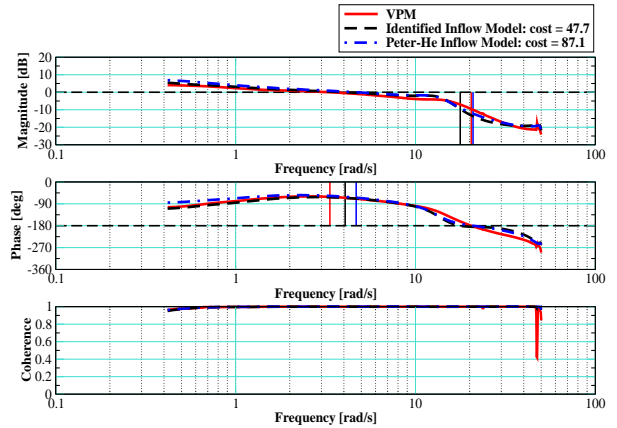
Figure 49: Stability margin assessment of the broken-loop response, $f(s)/e(s)$, for the longitudinal channel, 80 knots